Supporting Information: Controlling photothermal forces and backaction in nano-optomechanical resonators through strain engineering

Menno H. Jansen,[†] Cauê M. Kersul,[‡] and Ewold Verhagen[*,†]

[†]*Center for Nanophotonics, AMOLF, Amsterdam, The Netherlands*

[‡]*Centro de Tecnologia da Informação Renato Archer, Campinas, Brazil*

E-mail: verhagen@amolf.nl

Number of pages: 21

Number of tables: 3

Number of figures: 5

Supplementary Section 1 Fabrication

The devices are fabricated using a standard E-beam lithography (EBL) process on a silicon-on-insulator (SOI) platform. First, a wafer with a 220 nm Si device layer, on top of 3 µm buried oxide and a thick Si substrate, is diced into 12x20 mm chips. The chip is cleaned with base piranha ($H_2O/30\%NH_4OH/30\%H_2O_2$ 5:1:1 mixture). After this, a 100 nm layer of hydrogen silsesquioxane (HSQ) is spincoated on top. The chip is then cleaved to provide an edge with flat resist to which the devices will be aligned. This makes them accessible with a lensed fiber. The device geometry is then patterned in the resist aligned to the cleaved edge using a Raith Voyager EBL system, followed by development. This pattern is then etched into the Si device layer using Inductively Coupled Plasma Reactive Ion Etching (ICP RIE) in an Oxford Instruments PlasmaPro 100 Cobra with HBr/O_2 chemistry. Finally, the devices are underetched by hydrofluoric acid (HF) vapor etching using an SPTS µEtch. This simultaneously removes the leftover HSQ resist. Figure S1 shows an overview of resulting devices with various asymmetries. Two zipper cavities (with slightly different scaling and thus optical frequencies) are positioned next to each feed waveguide to increase the number of devices that can be studied.

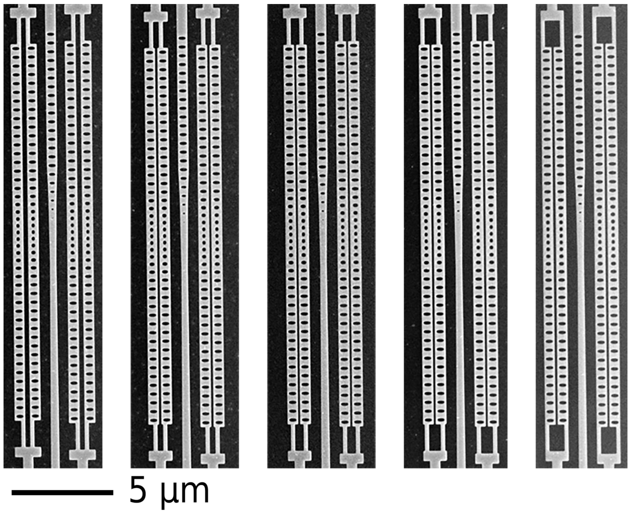

Figure S1: Overview of used devices. The asymmetry parameter A varies from -1 to +1 from left to right in steps of 0.5.

One aspect that can be seen in Figure S1 is that for negative asymmetry we generally use devices with larger gaps separating the two beams of the zipper cavity than for positive asymmetry. This is because of residual stress in the SOI wafers that we encountered in earlier fabrication runs. Due to asymmetric attachment, the tensile stress would pull the two beams of negative asymmetry devices toward each other, causing the beams of devices with gaps below 150 nm to collapse. For positive asymmetry devices, smaller gaps can be realized. While this variation leads to variations in optomechanical coupling rate g_0, we compensate for this in the analysis as described in the main text. We note that the amount of tensile stress depends on the location of the chip in the wafer, which means that the impact of stress can vary from chip to chip.

Supplementary Section 2 Device parameters

Table S1 lists the mechanical frequencies and linewidths of the devices used. Table S2 lists the optical frequencies and linewidths of the cavity modes used. The uncertainty in the resonance frequencies is not listed, as it is on the order of ten Hz for the mechanical modes and MHz for the optical modes. The used gap sizes, along with simulated and measured values of g_0 for both modes, are listed in Table S3.

Table S1: Mechanical parameters of the devices used in this work.

A	$\Omega/2\pi$ (MHz)	$\Gamma/2\pi$ (Hz)
-1	5.767	144 ± 4
-0.5	5.752	160 ± 3
0	5.646	140 ± 2
0.5	5.760	142 ± 2
1	5.896	144 ± 2

Supplementary Section 3 Setup

The characterization of all devices was performed using the setup depicted in Figure S2. The light source is a Toptica CTL 1550 tunable laser with a wavelength range from 1510 to 1630

Table S2: Optical parameters of the devices used in this work.

A	Opt. symm.	$\omega/2\pi$ (THz)	$\kappa/2\pi$ (GHz)	$\kappa_1/2\pi$ (GHz)	$\kappa_2/2\pi$ (GHz)
-1	Even	192.027	3.824 ± 0.132	0.54 ± 0.11	3.24 ± 0.32
	Odd	192.495	2.795 ± 0.009	0.52 ± 0.06	2.26 ± 0.11
-0.5	Even	186.933	3.344 ± 0.095	1.34 ± 0.24	1.87 ± 0.24
	Odd	188.184	4.294 ± 0.074	1.98 ± 0.09	2.22 ± 0.09
0	Even	187.360	4.525 ± 0.029	1.83 ± 0.07	2.70 ± 0.07
	Odd	188.308	4.686 ± 0.043	2.13 ± 0.03	2.58 ± 0.03
0.5	Even	189.875	3.669 ± 0.003	1.46 ± 0.14	2.21 ± 0.14
	Odd	190.760	4.271 ± 0.021	1.94 ± 0.08	2.33 ± 0.08
1	Even	189.848	3.899 ± 0.003	1.67 ± 0.06	2.22 ± 0.06
	Odd	190.673	4.277 ± 0.011	1.95 ± 0.04	2.36 ± 0.04

Table S3: Optomechanical parameters of the devices used in this work.

A	Gap (nm)	Opt. symm.	Simulated $g_0/2\pi$ (kHz)	Measured $\|g_0\|/2\pi$ (kHz)
-1	260	Even	-69.5	104.2 ± 2.4
		Odd	38.4	19.8 ± 0.4
-0.5	175	Even	-190.1	164.1 ± 2.5
		Odd	50.5	20.4 ± 2.7
0	200	Even	-143.7	140.1 ± 0.4
		Odd	45.7	24.2 ± 0.1
0.5	200	Even	-132.9	128.0 ± 0.9
		Odd	54.5	46.7 ± 2.5
1	200	Even	-134.1	120.0 ± 0.4
		Odd	49.8	46.0 ± 3.5

nm. A 90:10 fiber beamsplitter splits the laser light into a local oscillator (LO) and signal arm. The intensity of the light in the signal arm is stabilized using a PID controller. With a subsequent variable optical attenuator (VOA), the power can be reduced electronically to enable power sweeps. This light is then routed through a circulator and coupled into the device using a lensed fiber.

The device is fabricated on a chip which is mounted on the cold finger of a Montana Cryostation C2 cryostat. The chip on which the devices are situated is clamped to the cold finger of the cryostat, with thermal grease on the interface. The thermometer that is used to measure the temperature is clamped in the same way, and should therefore be thermalized similarly. Additionally, there is a radiation shield in the cryostat, which is also at 30K, such that the radiation environment that the sample sees is at the same temperature.

The same lensed fiber collects the reflected light, which, depending on detuning, has entered the cavity and has had the mechanical motion imprinted on its phase. The local oscillator arm goes through a dual parallel phase-modulated Mach-Zehnder interferometer (DPMZI), which displaces the frequency of the light by 40 MHz by single-sideband modulation. The light from both arms is coupled into free space, where their polarizations are rotated such that they are orthogonal before passing through the first polarizing beamsplitter (PBS), and then rotated by 45° before passing through the second PBS. That PBS splits the light fields such that they can interfere on both arms of the balanced detector. The electronic spectrum analyzer (ESA) then takes the Fourier transform of the differential photocurrent, giving us our mechanical spectra.

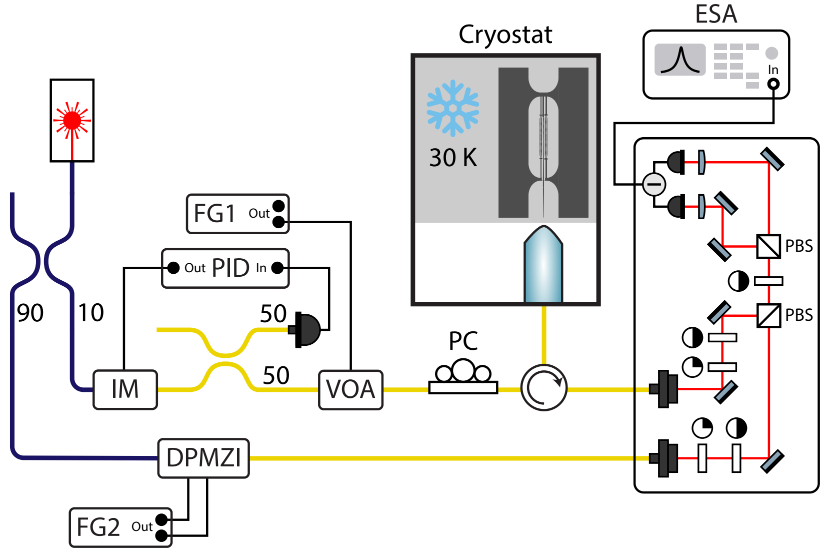

Figure S2: Experimental setup. PID: PID controller. FG: Function generator. IM: Intensity modulator. VOA: Variable optical attenuator. PC: Polarization controller. DPMZI: Dual parallel phase-modulated Mach-Zehnder interferometer. ESA: Electronic spectrum analyzer.

Supplementary Section 4 Data Analysis

In this subsection, we will describe the data analysis steps that yield the final normalized linewidth variation $\beta_{\Gamma,\mathrm{dyn}}/(|g_0|\beta_{\Omega,\mathrm{stat}})$ that is plotted in Figure 4a and discussed in the main text. The different steps are shown in the panels of Figure S3. Firstly, we perform a wavelength sweep over the optical mode at fixed input power, recording the mechanical spectrum at each wavelength. An example of such a sweep for the $A = -1$ device is shown in Figure S3a. At each wavelength, the mechanical frequency and linewidth are determined using a fit, as shown in Figure S3b. Plotting the frequency (linewidth) at each detuning yields the blue (orange) data in Figure S3c (d), with the error bars determined from the covariance matrix of the least squares fit. We can now fit this data with a symmetric and anti-symmetric component, being the optical Lorentzian response and derivative of this Lorentzian, for the static and dynamic contributions, respectively:

$$\Omega = \Omega_0 + \delta\Omega_{\text{drift}} \cdot \Delta + \delta\Omega_{\text{dyn}} \cdot \frac{32}{3\sqrt{3}} \cdot \frac{\kappa^3 \cdot \Delta}{\left(4\Delta^2 + \kappa^2\right)^2} + \delta\Omega_{\text{stat}} \cdot \frac{\kappa^2}{4\Delta^2 + \kappa^2} \tag{S1}$$

$$\Gamma = \Gamma_0 + \delta\Gamma_{\text{dyn}} \cdot \frac{32}{3\sqrt{3}} \cdot \frac{\kappa^3 \cdot \Delta}{\left(4\Delta^2 + \kappa^2\right)^2} + \delta\Gamma_{\text{stat}} \cdot \frac{\kappa^2}{4\Delta^2 + \kappa^2}. \tag{S2}$$

Here, the prefactors originate from normalization to facilitate fitting directly to the experimental data, without requiring external quantities, allowing calibrations of powers and efficiencies to be done separately. As an example, in the bad cavity limit ($\Omega \ll \kappa$) the expression for the dynamical frequency variation, due to the optical spring effect, is given by[1]

$$\delta\Omega_m(\Delta) \approx g_0^2 n_{\text{ph}}(\Delta) \frac{2\Delta}{\Delta^2 + \kappa^2/4}. \tag{S3}$$

We fill in $n_{\text{ph}}(\Delta) = \frac{P_{in}}{\hbar\omega_L} \frac{\kappa_{ex}}{\Delta^2 + \kappa^2/4}$, solve for the maximum at $\frac{\partial\delta\Omega_m}{\partial\Delta} = 0$, and use the value found to normalize the $\delta\Omega_{dyn}$ term in Equation S1.

An example of this fit is shown in Figure S3c and d for frequency and linewidth, respectively. The optical resonance frequency and linewidth are determined separately from a fit to the area of the mechanical peak, and kept fixed for these fits. The static contribution is plotted in red, and the dynamic contribution in green. Repetition of this procedure at multiple powers gives the data points that belong to one device in Figure S3e - l. The error bars represent standard errors obtained from the covariance of the fit parameters. From a linear fit to these points, we can then get the slopes $\beta_{\{\Omega,\Gamma\},\{dyn,stat\}}$.

The final quantity required for normalization in Figure 4a is g_0, which we can calculate from $\beta_{\Omega,dyn}$ with $|g_0| = \sqrt{\frac{4}{3\sqrt{3}}\beta_{\Omega,dyn}\kappa}$.

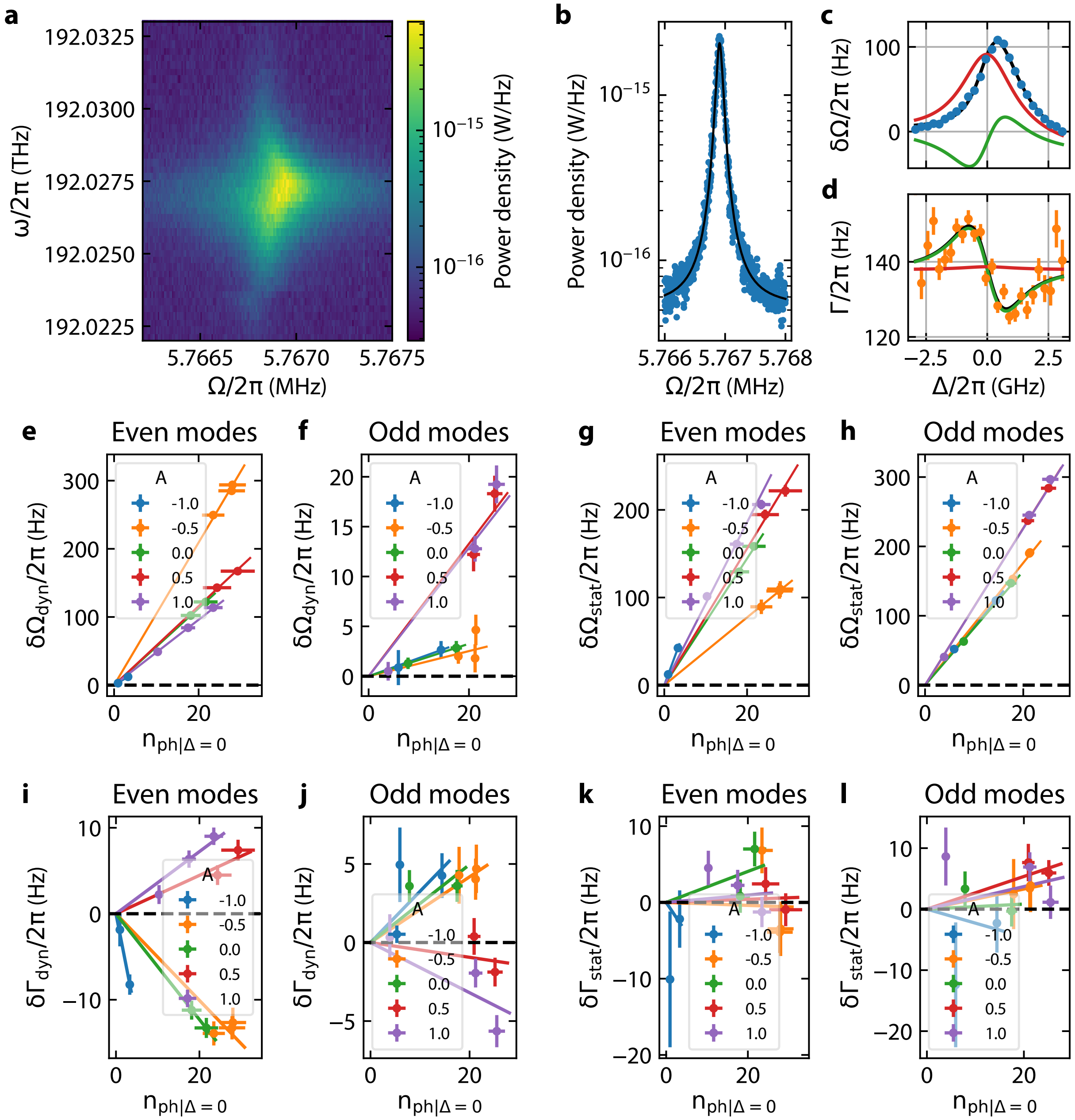

Figure S3: **a** Optical frequency sweep of the device with $A = -1$. **b** Mechanical spectrum at one optical frequency. **c**, **d** Extracted mechanical frequency and linewidth as function of optical detuning, with symmetric static (red) and anti-symmetric dynamic (green) components of the fit (black). **e-l** Extracted dynamic and static frequency and linewidth contributions for all asymmetries A as a function of peak cavity photon number.

Supplementary Section 5 Theoretical model

Here we extend the discussion on the mechanisms behind the photothermal backaction cycle discussed in the main text, by reviewing the model established in Primo *et al.*[2] The dynamics of the optical and mechanical modes are treated in the standard optomechanical way, with lumped element coupled mode theory equations, where the coupling rates are given by overlap integrals of the optical and mechanical fields.[3]

The first step in the modeling consists of knowing how an arbitrary oscillating temperature field drives the mechanical mode of interest, from[2] we have

$$m_{\text{eff}}\big(\delta\ddot{x} + \Gamma\delta\dot{x} + \Omega^2\delta x\big) = \int \boldsymbol{S}^x(\vec{r})\text{:}\,\big(\boldsymbol{c}\text{:}\boldsymbol{S}^\theta(\vec{r},t)\big)\,dV, \tag{S4}$$

where δx represents the amplitude of fluctuations in the mechanical mode, m_{eff}, Γ, and Ω are its effective mass, decay rate, and angular frequency, $\boldsymbol{c}$ is the stiffness tensor of the medium, the operator ":" is the tensor contraction operation, $\boldsymbol{S}^x(\vec{r})$ is the normalized strain profile of the mechanical mode of interest and $\boldsymbol{S}^\theta(\vec{r},t)$ is the thermal strain profile, which is given by

$$\boldsymbol{S}^\theta(\vec{r},t) = \boldsymbol{\alpha}\delta T(\vec{r},t), \tag{S5}$$

where $\boldsymbol{\alpha}$ is the thermal expansion tensor and $\delta T(\vec{r},t)$ is the temperature fluctuation profile. Examples of $\boldsymbol{S}^x(\vec{r})$ for various values of asymmetry parameter A are shown in Figure S4. Comparing the strain profiles at the extremities near the asymmetric tethers, the geometries with negative A show more positive strain, whereas at positive A, the strain is more negative. This pattern also extends toward the middle of the beam, but here the perturbation from the asymmetry is overshadowed by the main contribution from the doubly clamped beam mode itself. The perturbation merely yields a slight asymmetry in the strain profile of a cross-section, as seen in Figure 2e in the main text.

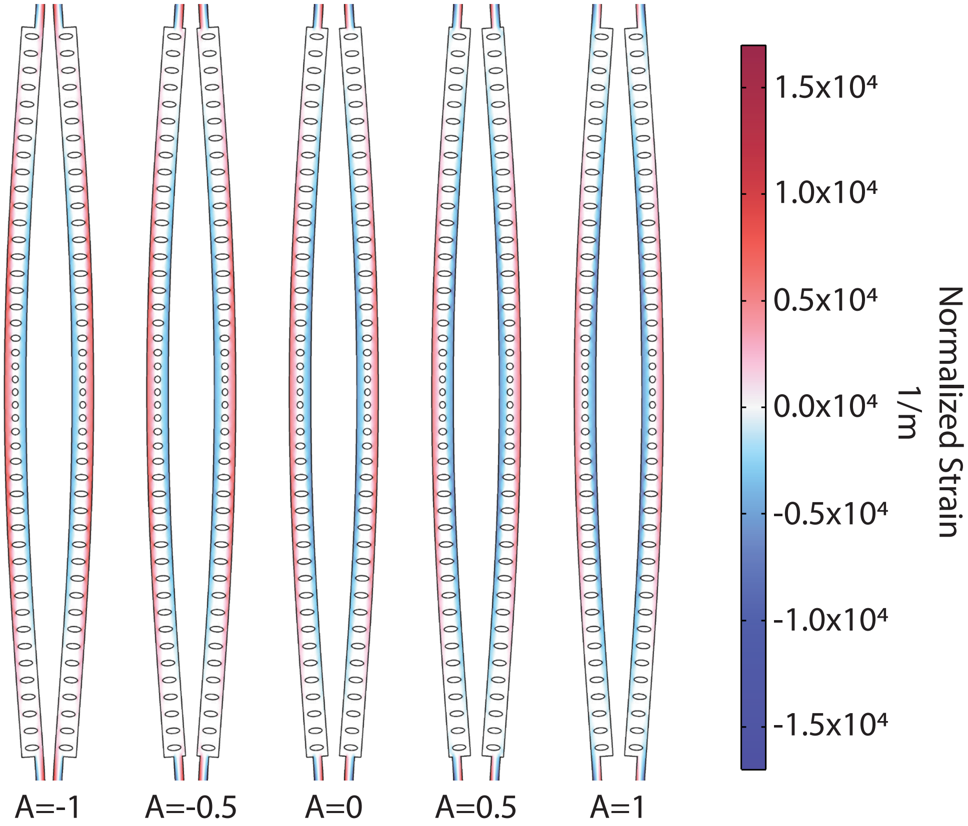

Figure S4: Strain profiles, normalized by the maximal absolute displacement, of geometries with varying asymmetry parameter A.

In the case of the photothermal backaction $\delta T(\vec{r},t)$ is generated by the photon number fluctuations, following the equation for diffusive heat transport:

$$c_p\rho\partial_t\delta T(\vec{r},t) = \nabla\cdot\big(k_{\mathrm{th}}\nabla\delta T(\vec{r},t)\big) + \dot{Q}(\vec{r},t), \tag{S6}$$

where c_p, ρ and k_{th} are, respectively, the specific heat, the mass density, and the thermal conductivity of the medium. $\dot{Q}$ is the fluctuating heat source due to the optical absorption.

In order to link $\dot{Q}(\vec{r},t)$ to the optical mode amplitude fluctuations we will first remember that the total heating power integrated over the device area should be equal to the energy absorption rate of the cavity:

$$\int_{V_{\mathrm{abs}}}\dot{Q}_t(\vec{r})dV = \kappa_{abs}\hbar\omega_0|a|^2, \tag{S7}$$

where a is the optical amplitude, κ_{abs} is the optical absorption rate and ω_0 is the angular optical frequency. Now we assume that the absorptive loss is linear and homogeneous across the entire device volume. We also assume it is proportional to the local electrical energy density of the optical field — here we could have assumed that the linear absorption is localized partially or completely in the surface, arriving at similar final conclusions, with the only change being the domain over which to evaluate the integral — leading us to the following expression for the local heating density:

$$\dot{Q}_t(\vec{r}) = \frac{\kappa_{abs}\,\varepsilon_r(\vec{r})|\vec{e}(\vec{r})|^2}{\int_{V_{\text{abs}}}\varepsilon_r(\vec{r})|\vec{e}(\vec{r})|^2 dV}\hbar\omega_0|a|^2, \tag{S8}$$

where $\varepsilon_r(\vec{r})$ is the medium dielectric constant, $\vec{e}(\vec{r})$ is the normalized optical electric field, and $\int_{V_{\text{abs}}}$ indicates integration over the region of the device where absorption occurs. The above expression is independent of the choice of normalization for the electric field, as the same $|\vec{e}(\vec{r})|^2$ appears in both the denominator and the numerator.

When we consider that the optical mode amplitude varies over time with a small fluctuation, $a(t) = a_0 + \delta a(t)$, we can perform small signal analysis, leading to:

$$\dot{Q}_0(\vec{r}) + \dot{Q}(\vec{r},t) = \frac{\kappa_{abs}\,\varepsilon_r(\vec{r})|\vec{e}(\vec{r})|^2}{\int_{V_{\text{abs}}}\varepsilon_r(\vec{r})|\vec{e}(\vec{r})|^2 dV}\hbar\omega_0\left(|a_0|^2 + a_0^*\delta a(t) + a_0\delta a^*(t) + |\delta a(t)|^2\right), \tag{S9}$$

where $\dot{Q}_0(\vec{r})$ is the constant heating power density and $\dot{Q}(\vec{r,t})$ the term containing the fluctuations.

Finally ignoring $|\delta a(t)|^2$ because it is much smaller than $a_0^*\delta a(t) + a_0\delta a^*(t)$ we arrive at the following expression for the fluctuating heat source, defined inside the region in space where absorption occurs:

$$\dot{Q}(\vec{r},t) = \frac{\kappa_{\text{abs}}\,\varepsilon_r(\vec{r})|\vec{e}(\vec{r})|^2}{\int_{V_{\text{abs}}}\varepsilon_r(\vec{r})|\vec{e}(\vec{r})|^2 dV}\,\hbar\omega_0\left(a_0^*\delta a(t) + a_0\delta a^*(t)\right), \tag{S10}$$

The term $(a_0^*\delta a(t) + a_0\delta a^*(t))$ approximates the linearized photon number fluctuations $\delta n(t)$, assuming that the overall fluctuations are small compared to the mean photon number $|a_0|^2$.

Indeed Equation S6 is a linear nonhomogeneous partial differential equation. The standard procedure to solve such equation is to start by finding the solution to the homogeneous part of the equation, setting $\dot{Q}(\vec{r},t) = 0$:

$$c_p\rho\partial_t\delta T(\vec{r},t) = \nabla\cdot\big(k_{\text{th}}\nabla\delta T(\vec{r},t)\big), \tag{S11}$$

We can find solutions to this equation using the technique of variable separation where we assume that the solution is a product of functions which depend separately on time and position, $\delta T(\vec{r},t) = \delta\theta(t)\tilde{T}(\vec{r})$. Applying such assumption on Equation S12 we can arrive at:

$$\frac{\partial_t\delta\theta(t)}{\delta\theta(t)} = \frac{\nabla\cdot\big(k_{\text{th}}\nabla\tilde{T}(\vec{r})\big)}{c_p\rho\,\tilde{T}(\vec{r})}, \tag{S12}$$

The left side of the above equation depends uniquely on the time, while the right side depends on position. This is only possible if both sides are equal to a constant, which we will, conveniently, call here $-1/\tau$ arriving at the following two equations:

$$\begin{aligned} \partial_t\delta\theta(t) &= -\frac{1}{\tau}\delta\theta(t), \\ \frac{1}{\tau}c_p\rho\tilde{T}(\vec{r}) &= -\nabla\cdot\big(k_{\text{th}}\nabla\tilde{T}(\vec{r})\big), \end{aligned} \tag{S13}$$

The first is simply a ordinary differential equation in time, whose solution is $\delta\theta(t) = \delta\theta(0)e^{-t/\tau}$, while the second is a partial differential equation in position. This is essentially a Sturm-Liouville problem,[4] where $1/\tau_k$ and $\tilde{T}_k(\vec{r})$ are respectively the eigenvalues and the associated eigenmodes. Assuming fixed temperature or constant heat flow at the boundaries of the considered domain it can be shown that both operators $\nabla\cdot(k_{\text{th}}\nabla)$ and $c_p\rho$ in this equation are Hermitian, with the latter being positive definite, in such a way that the equation has a complete set of orthogonal eigenmodes. Each eigenmode has a typical timescale given by its associated τ_k. Lower-order modes have a larger τ_k, i.e. a slower response time.

As the basis formed by the eigenmodes $\tilde{T}_k$ is complete the solution of the more general non-homogeneous problem can be written as a sum over it:

$$\delta T(\vec{r},t) = \sum_k \delta\theta_k(t)\tilde{T}_k(\vec{r}), \tag{S14}$$

where $\delta\theta_k(t)$ represents the amplitude of the k-th thermal mode and $\tilde{T}_k(\vec{r})$ represents its normalized profile.

Applying Equation S14 in Equation S6 and using the properties of this complete set of eigenmodes one can derive dynamic equations for the amplitude, $\theta_k(t)$, of each thermal mode:

$$\delta\dot{\theta}_k = -\frac{1}{\tau_k}\delta\theta_k + \frac{\int \dot{Q}(\vec{r},t)\tilde{T}_k(\vec{r})dV}{\int c_p\rho\tilde{T}_k^2(\vec{r})dV}, \tag{S15}$$

where τ_k is the thermal decay time for the k-th mode. Applying Equation S10 on the right-hand side of Equation S15 the dynamic equation can be written as:

$$\delta\dot{\theta}_k = -\frac{1}{\tau_k}\delta\theta_k + \frac{\hbar\omega_0\kappa_{\text{abs}}R_k^\theta}{\tau_k}\left(a_0^*\delta a + a_0\delta a^*\right), \tag{S16}$$

where the thermal resistance of the k-th mode is defined as:

$$R_k^\theta = \tau_k\frac{\int_{V_{\text{abs}}}\varepsilon_r|\vec{e}|^2\tilde{T}_k dV}{\int_{V_{\text{abs}}}\varepsilon_r|\vec{e}|^2 dV\int c_p\rho\tilde{T}_k^2 dV}, \tag{S17}$$

The same modal expansion of the temperature field is performed on the right-hand side of Equation S4:

$$\int \boldsymbol{S}^x(\vec{r}) \colon \left(\boldsymbol{c} \colon \boldsymbol{S}^\theta(\vec{r},t)\right) dV = \Lambda_k^\theta\delta\theta_k(t), \tag{S18}$$

where Λ_k^θ is the thermo-elastic coupling between the k-th thermal mode and the mechanical mode:

$$\Lambda_k^\theta = \int \mathbf{S}^x : (\mathbf{c} : \boldsymbol{\alpha})\,\tilde{T}_k\,dV \tag{S19}$$

As such, the full set of lumped parameter equations for the coupled dynamics of the optical, mechanical, and thermal mode fluctuations is given by

$$\begin{aligned}
\delta\dot{a} =& iG_x \delta x a_0 + (i\Delta_0 - \frac{\kappa}{2})\delta a, \\
\delta\ddot{x} + \Gamma\delta\dot{x} + \Omega^2\delta x =& \frac{\hbar G_x}{m_{\text{eff}}}(a_0^*\delta a + a_0\delta a^*) + \sum_k \frac{\Lambda_k^\theta}{m_{\text{eff}}}\delta\theta_k, \\
\delta\dot{\theta}_k =& -\frac{1}{\tau_k}\delta\theta_k + \frac{\hbar\omega_0\kappa_{\text{abs}}R_k^\theta}{\tau_k}(a_0^*\delta a + a_0\delta a^*),
\end{aligned} \tag{S20}$$

where κ is the total optical decay rate, G_x is the optomechanical coupling (the normalized optomechanical coupling is given by $g_0 = G_x\sqrt{\frac{\hbar}{2m_{\text{eff}}\Omega}}$) and $\Delta_0 = \omega_l - \omega_0$ is the detuning between the angular frequencies of the laser, ω_l, and of the optical mode ω_0.

These linearized equations can be solved in the frequency domain:

$$\begin{aligned}
\left[(\Delta_0 + \omega) + i\frac{\kappa}{2}\right]\delta a(\omega) =& -G_x\delta x(\omega)a_0, \\
\left[(\Omega^2 - \omega^2) - i\omega\Gamma\right]\delta x(\omega) =& \frac{\hbar G_x}{m_{\text{eff}}}\left[a_0^*\delta a(\omega) + a_0[\delta a]^*(\omega)\right] + \sum_k \frac{\Lambda_k^\theta}{m_{\text{eff}}}\delta\theta_k(\omega), \\
\left(-i\omega + \frac{1}{\tau_k}\right)\delta\theta_k(\omega) =& \frac{\hbar\omega_0\kappa_{\text{abs}}R_k^\theta}{\tau_k}\left[a_0^*\delta a(\omega) + a_0[\delta a]^*(\omega)\right].
\end{aligned} \tag{S21}$$

Using the fact that $\delta x(t)$ and $\delta\theta(t)$ are real variables, these equations can be solved in such a way that the equation for mechanical dynamics can be written as:

$$m_{\text{eff}}\left[(\Omega^2 - \omega^2) - i\omega\Gamma\right]\delta x(\omega) = -\left(\hbar G_x + \hbar\omega_0\kappa_{\text{abs}}\sum_k \frac{\Lambda_k^\theta R_k^\theta \chi_k^\theta(\omega)}{\tau_k}\right)\Psi(\omega,\Delta_0)|a_0|^2 G_x\delta x(\omega), \tag{S22}$$

where

$$\chi_k^\theta(\omega) = \frac{1}{1/\tau_k - i\omega} \tag{S23}$$

is the thermal susceptibility of the k-th mode and

$$\Psi(\omega,\Delta_0) = \frac{1}{(\Delta_0 + \omega) + i\frac{\kappa}{2}} + \frac{1}{(\Delta_0 - \omega) - i\frac{\kappa}{2}}, \tag{S24}$$

is the symmetrized optical susceptibility.

The left-hand side of Equation S22 is essentially the inverse of the bare mechanical susceptibility $\chi_m^{-1}(\omega) = m_{\text{eff}}\left[(\Omega^2-\omega^2) - i\Gamma\omega\right]$. As such, the right-hand side, which is also proportional to $\delta x(\omega)$, can be seen as optomechanical ($\Sigma^{\text{RP}}(\omega, \Delta_0)$) and photothermal ($\Sigma^{\theta}(\omega, \Delta_0)$) contributions to a "dressed" inverse mechanical susceptibility:

$$\chi_{m,\text{eff}}^{-1}(\omega) = \chi_m^{-1}(\omega) + \Sigma^{\text{RP}}(\omega) + \Sigma^{\theta}(\omega), \tag{S25}$$

where

$$\Sigma^{\text{RP}}(\omega, \Delta_0) = \hbar (G_x)^2 \Psi(\omega, \Delta_0)|a_0|^2, \tag{S26a}$$

$$\Sigma^{\theta}(\omega, \Delta_0) = \hbar \omega_0 \kappa_{\text{abs}} \sum_k \frac{R_k^{\theta} \Lambda_k^{\theta} \chi_k^{\theta}(\omega)}{\tau_k} G_x \Psi(\omega, \Delta_0)|a_0|^2. \tag{S26b}$$

In order to simplify our notation, it is useful to define here an "effective photothermal coupling" accounting for the multiple thermal modes, where all the calculated overlap integrals related to the photothermal interaction are lumped together:

$$G_{\text{pt}}(\omega) = \omega_0 \kappa_{\text{abs}} \sum_k \frac{R_k^{\theta} \Lambda_k^{\theta} \chi_k^{\theta}(\omega)}{\tau_k}. \tag{S27}$$

This effective response can be used, for example, to define the equivalent single-photon photothermal force as $\hbar G_{\text{pt}}(\omega)$ that can be more straightforwardly compared to the optomechanical single photon force $\hbar G_x$.

In the weak coupling regime discussed here, both $\Sigma^{\text{RP}}(\omega)$ and $\Sigma^{\theta}(\omega)$ are more or less constants over the regions where the mechanical susceptibility is relevant — a band of size Γ around the frequency Ω. As such, the effect of the coupling is to change the mechanical frequency and linewidth:

$$\Omega_{\text{eff}} = \Omega + \delta\Omega \tag{S28a}$$

$$\Gamma_{\text{eff}} = \Gamma + \delta\Gamma, \tag{S28b}$$

where

$$\delta\Omega = \frac{1}{2m_{\text{eff}}\Omega}\text{Re}\left[\Sigma^{\text{RP}}(\Omega,\Delta_0) + \Sigma^{\theta}(\Omega,\Delta_0)\right], \tag{S29a}$$

$$\delta\Gamma = \frac{-1}{m_{\text{eff}}\Omega}\text{Im}\left[\Sigma^{\text{RP}}(\Omega,\Delta_0) + \Sigma^{\theta}(\Omega,\Delta_0)\right]. \tag{S29b}$$

The real and imaginary parts of the above expressions are related to the in-phase and in-quadrature responses of the backaction loops evaluated at frequency Ω. The in-phase response generates a conservative force, which only affects the mechanical frequency, while the in-quadrature response is related to dissipative forces which affect the mechanical linewidth.

Separating optomechanical and photothermal contributions to the linewidth variation, we arrive at

$$\delta\Gamma^{\text{RP}} = -\frac{\hbar(G_x)^2|a_0|^2}{m_{\text{eff}}\Omega}\text{Im}\left[\Psi(\Omega,\Delta_0)\right] \tag{S30a}$$

$$\delta\Gamma^{\theta} = -\frac{\hbar G_x|a_0|^2}{m_{\text{eff}}\Omega}\text{Im}\left[G_{\text{pt}}(\Omega)\Psi(\Omega,\Delta_0)\right], \tag{S30b}$$

For the optomechanical contribution only the delay given by the optical response is relevant, while for the photothermal contribution both the optical and thermal responses are present. Our devices operate in the unresolved sideband regime $\Omega \ll \kappa$, where the mechanical time scale is much slower than the optical time scale. In this regime, we have $\text{Im}\left[\Psi(\Omega,\Delta_0)\right] \ll \text{Re}\left[\Psi(\Omega,\Delta_0)\right]$, and as such $\delta\Gamma^{\text{RP}}$ is much smaller than $\delta\Omega^{\text{RP}}$.

The comparison between the mechanical and thermal timescales is less straightforward, as we have multiple thermal modes. In Figure S5**d** we present the contributions of different thermal modes to the overall effective photothermal coupling, $G_{\mathrm{pt}}(\Omega)$. For instance, the contribution of the fourth thermal mode is already 80 times smaller than the contribution from the first one, indicating that indeed only the slow thermal modes are relevant in our analysis. In Figure S5**a**, **b** and **c**, we break the main contributions to $G_{\mathrm{pt},k}(\Omega)$ in 3 terms.

The first term is the thermal resistance divided by τ_k, R_k^θ/τ_k which is essentially the overlap between the spatial temperature profile and the electrical energy density. As we consider higher order thermal modes with higher τ_k^{-1}, it falls very slowly. This happens because the optical mode is concentrated to the scale of a few holes at the center of the nanobeam, and the initial thermal modes are very similar in this central region, presenting a nearly homogeneous profile across the cross-section. This can be seen when we compare the first ($k = 1$) and second ($k = 2$) order modes at Figure S5**e**. As we approach $\tau_k^{-1} = 10^{10}$ we see an abrupt fall, associated with the appearance of modes like the one shown in the right side of Figure S5**e** ($k = 44$), which present an odd-like temperature profile along the nanobeam cross-section.

The second term is the thermo-elastic coupling Λ_k^θ, the overlap integral between the thermal and mechanical fields is shown in Figure S5**b**. As the mechanical mode is more distributed about the longitudinal direction of the nanobeam the reduction of Λ_k^θ with increasing complexity of the thermal mode is more pronounced than for R_k^θ/τ_k. One interesting thing is that as we approach $\tau_k^{-1} = 10^{10}$ there is a sharp increase in the coupling strength, and again this is because of the appearance of odd-like modes across the cross section like the one shown in Figure S5**e** for $k = 44$, which has a better overlap with the odd-like strain profile of the mechanical mode.

Finally we have the contribution from the imaginary part of the thermal susceptibility, $\chi_k^\theta(\Omega)$ (Equation S23), which is directly related to the thermal response delay discussed previous. This contribution is shown in Figure S5**c**. For τ_k^{-1} below the mechanical frequency we have a plateau, indicating that the thermal response is in quadrature with the mechanical mode, with the delay approaching a maximum. For τ_k^{-1} above the mechanical frequency the thermal mode follows the mechanical mode more closely and the delay is smaller, leading to progressively smaller mechanical linewidth variation effects.

Analyzing the trends presented in Figure S5**a**, **b**, and **c**, we see that the thermal susceptibility is the dominant factor to determine which thermal modes have a larger contribution, as Λ_k^θ and R_k^θ/τ_k present opposite trends with regard to the symmetry of the thermal modes across the nanobeam cross section. In summary ,in principle, we can have many thermal modes with arbitrarily small thermal response times. However, the nature of the thermal susceptibility is such that modes for which $\Omega\tau_k \ll 1$ are irrelevant.

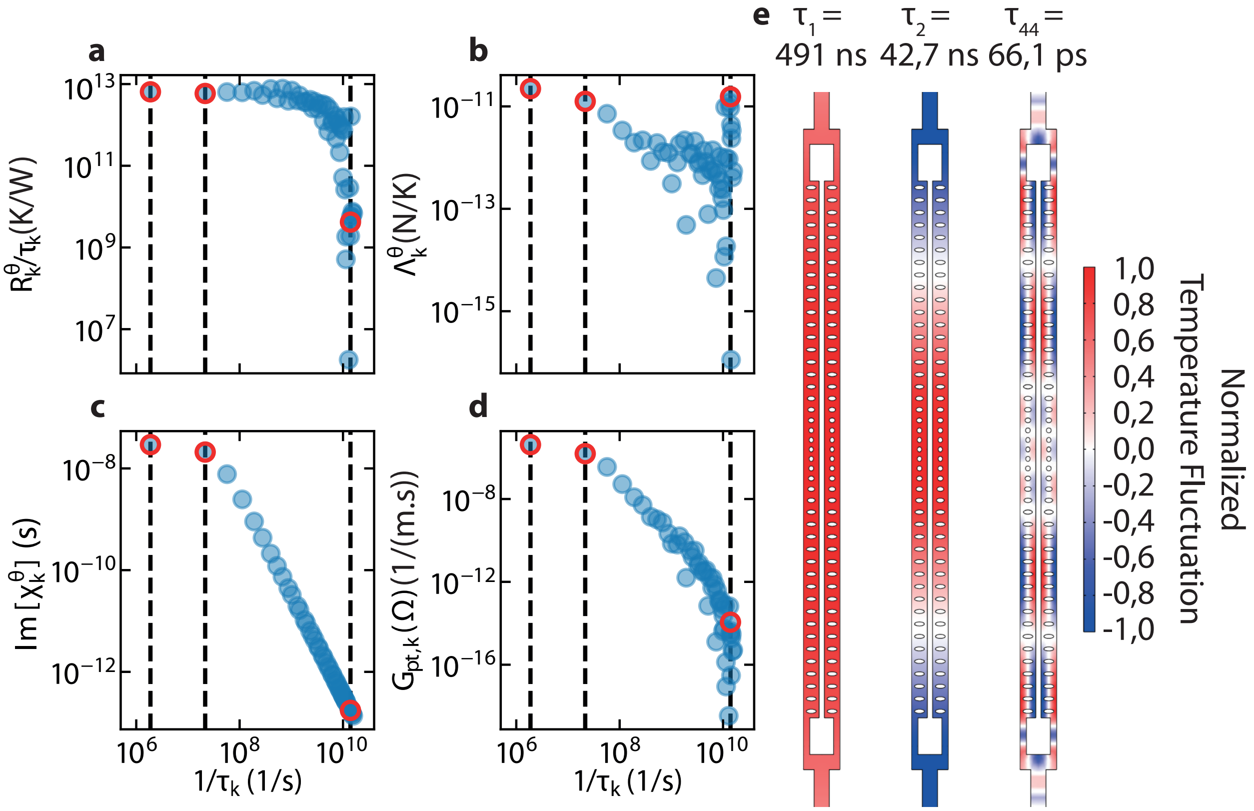

Figure S5: This figure presents information about how the first 50 thermal modes contribute to the overall photothermal effect for the $A = -1$ device. **a** Thermal resistance divided by the thermal decay time for the k-th thermal mode. **b** Thermo-elastic coupling of the k-th thermal mode. **c** Imaginary part of the thermal susceptibility of the k-th thermal mode. **d** Effective photo-thermal coupling, $G_{\mathrm{pt},k}(\Omega)$. The $x-$axis presents the decay time of the respective thermal modes. **e** Temperature profiles for the first, second and forty fourth thermal mode with its respective decay times, which are highlighted in panels **a**, **b**, **c** and **d**.

We know from simulations that the response of those modes is much slower than the mechanical timescale $1/\tau_k \ll \Omega$. In this regime some simplifications can be made (here we have used the fact that in Eq.S17 R_k^θ is proportional to τ_k and the assumption $1/\tau_k \ll \Omega$):

$$G_{\mathrm{pt},k}(\Omega) = \omega_0 \kappa_{\mathrm{abs}} \frac{R_k^\theta \chi_k^\theta(\Omega) \Lambda_k^\theta}{\tau_k} \propto \frac{1}{\Omega^2 \tau_k} + i\frac{1}{\Omega}. \tag{S31}$$

As such, we affirm that $\frac{\mathrm{Im}[G_{\mathrm{pt},k}(\Omega)]}{\mathrm{Re}[G_{\mathrm{pt},k}(\Omega)]} \approx \Omega\tau_k \gg 1$.

Expanding the imaginary part in Equation S30b in terms of the real and imaginary parts of $G_{\mathrm{pt}}(\omega)$ and $\Psi(\Omega, \Delta_0)$ we arrive at

$$\delta\Gamma^\theta = -\frac{\hbar G_x |a_0|^2}{m_{\mathrm{eff}}\Omega} \left(\mathrm{Im}\left[G_{\mathrm{pt}}(\Omega)\right] \mathrm{Re}\left[\Psi(\Omega, \Delta_0)\right] + \mathrm{Re}\left[G_{\mathrm{pt}}(\Omega)\right] \mathrm{Im}\left[\Psi(\Omega, \Delta_0)\right]\right). \tag{S32}$$

The second term in the above expression is much smaller than the first because, as discussed previously, $\mathrm{Re}[G_{\mathrm{pt}}(\Omega)] \ll \mathrm{Im}[G_{\mathrm{pt}}(\Omega)]$ and $\mathrm{Im}\left[\Psi(\Omega, \Delta_0)\right] \ll \mathrm{Re}\left[\Psi(\Omega, \Delta_0)\right]$, and as such $\delta\Gamma^{\mathrm{RP}}$. As such,

$$\delta\Gamma^\theta \approx -\frac{\hbar G_x |a_0|^2}{m_{\mathrm{eff}}\Omega} \mathrm{Im}\left[G_{\mathrm{pt}}(\Omega)\right] \mathrm{Re}\left[\Psi(\Omega, \Delta_0)\right], \tag{S33}$$

indicating that for the photothermal backaction the dominant delay mechanism comes from the thermal dynamics.

Notice that in the regime $1/\tau_k \ll \Omega$ the size of the effect is nearly independent of the value of the thermal conductivity. This can be seen in Equation S31, where the dominant term i/Ω is not dependent on τ_k, which is the only parameter in our model dependent on thermal conductivity. In the regime considered here, we are assuming that within a single mechanical period heat has no time to flow. As such, the generated heat accumulates locally in such a way that the heating intensity is in quadrature with the temperature fluctuations.

Supplementary Section 6 Model limitations

As the temperature lowers, the overall number of phonons decreases, and with it phonon-phonon scattering interactions. As a consequence, the average phonon mean free path increases and with it silicon bulk conductivity. Indeed, the mean free path can become much larger than the device dimensions. In this case, the phonon scattering at the surface of the device becomes relevant. Usually, the scattering is diffuse because of surface roughness, characterizing the semi-ballistic regime, where the thermal behavior is yet diffusive, but the overall thermal conductivity depends on the device dimensions. At even lower temperatures, we can have specular scattering at the surface, when the typical phonon wavelength is much larger than the surface roughness. This defines the ballistic regime where heat transport is essentially wave-like.

To obtain a rough order-of-magnitude estimate of the typical mean free paths of the thermal phonons in our devices, we follow the approach laid out in Hauer *et al.*[5] Considering the temperature in which the experiments were realized, 30 K, the estimated phonon mean free path — this is a rough estimate of the mean free path assuming the simplified expression $\kappa_{\mathrm{th}} = \frac{1}{3}C_v v L$, where C_v is the specific heat, v is the average phonon speed in Silicon and L is the mean free path — is around 60 µm, which is much larger than the typical size of our device 220 nm, as such phonon scattering (calculated from $\frac{v\hbar}{2\pi k_b T}$) is dominated by surface scattering. The typical phonon wavelength is around 9 nm, which is of the same order of magnitude as the expected lateral surface roughness in silicon devices, which is around 5 nm, indicating that we are still in the semi-ballistic regime, but ballistic effects are not completely negligible.

Using the average width of the silicon with and without an elliptical hole in the horizontal direction $(170 + 500)/2$ nm $= 335$ nm and the thickness of 220 nm, we arrive at a typical typical mean free path for surface scattering given by $\sqrt{335 \cdot 220}$ nm $= 270$ nm. With this we can use the simplified expression $\kappa_{\mathrm{th}} = \frac{1}{3}C_v v L$ to estimate an effective thermal conductivity for the device $\kappa_{\mathrm{th}} = 23\,\mathrm{W/(K\,m)}$.

Aware of possible limitations, the results of our model were used as a guide to design the structures at 30 K. Ballistic effects related to differences in the surface properties between the inner and outer walls of the nanobeams could be one of the reasons behind the discrepancy between simulations and experiment.

References

(1) Aspelmeyer, M.; Kippenberg, T. J.; Marquardt, F. Cavity optomechanics. *Rev. Mod. Phys.* **2014**, *86*, 1391–1452.

(2) Primo, A. G.; Kersul, C. M.; Benevides, R.; Carvalho, N. C.; Ménard, M.; Frateschi, N. C.; de Assis, P.-L.; Wiederhecker, G. S.; Mayer Alegre, T. P. Accurate modeling and characterization of photothermal forces in optomechanics. *APL Photonics* **2021**, *6*, 086101.

(3) Wiederhecker, G. S.; Dainese, P.; Mayer Alegre, T. P. Brillouin optomechanics in nanophotonic structures. *APL photonics* **2019**, *4*.

(4) Guenther, R. B.; Lee, J. W. *Sturm-Liouville Problems: Theory and Numerical Implementation*, 1st ed.; CRC Press: Boca Raton, Florida : CRC Press, 2018. | Series: Monographs and research notes in mathematics, 2018.

(5) Hauer, B. D.; Clark, T. J.; Kim, P. H.; Doolin, C.; Davis, J. P. Dueling dynamical backaction in a cryogenic optomechanical cavity. *Physical Review A* **2019**, *99*, 053803.